

# Evaluating the representational power of pre-trained DNA language models for regulatory genomics

Ziqi Tang<sup>1</sup> and Peter K Koo<sup>1,\*</sup>

<sup>1</sup>Simons Center for Quantitative Biology, Cold Spring Harbor Laboratory, NY, USA

\*e-mail: [koo@cshl.edu](mailto:koo@cshl.edu)

## ABSTRACT

The emergence of genomic language models (gLMs) offers an unsupervised approach to learn a wide diversity of *cis*-regulatory patterns in the non-coding genome without requiring labels of functional activity generated by wet-lab experiments. Previous evaluations have shown pre-trained gLMs can be leveraged to improve prediction performance across a broad range of regulatory genomics tasks, albeit using relatively simple benchmark datasets and baseline models. Since the gLMs in these studies were tested upon fine-tuning their weights for each downstream task, determining whether gLM representations embody a foundational understanding of *cis*-regulatory biology remains an open question. Here we evaluate the representational power of pre-trained gLMs to predict and interpret cell-type-specific functional genomics data that span DNA and RNA regulation. Our findings suggest that current gLMs do not offer substantial advantages over conventional machine learning approaches that use one-hot encoded sequences. This work highlights a major limitation with current gLMs, raising potential issues in conventional pre-training strategies for the non-coding genome.

## Introduction

Large language models (LLMs) have demonstrated remarkable capabilities in natural language processing<sup>1-4</sup> and protein sequence analysis<sup>5-8</sup>. These LLMs, often termed “foundation models”, are trained through self-supervised learning to encode input data as contextual embeddings (also known as representations). The strength of pre-trained LLMs lies in the versatility of their embeddings, which can be leveraged for a broad spectrum of downstream predictive tasks. For instance, representations from pre-trained protein language models have been used to predict protein structures<sup>9-11</sup>, predict non-synonymous variant effects<sup>12,13</sup>, design novel protein sequences<sup>14-16</sup>, and study protein evolution<sup>17,18</sup>.

LLMs pre-trained on genomic DNA sequences offer a promising new paradigm to accelerate our understanding of functional elements in the non-coding genome<sup>19</sup>. Genomic language models (gLMs) could, in principle, help to understand the complex coordination of transcription factors (TFs) to control the activity of *cis*-regulatory elements (CREs). They might also enable more accurate predictions of the functional consequences of non-coding mutations, which can help to prioritize disease-associated variants. Additionally, gLMs capable of learning *cis*-regulatory rules could become instrumental in designing novel regulatory sequences with desirable functional properties. They might also facilitate functional comparisons of non-coding sequences across different species, a task currently complicated due to substantial evolutionary drift in non-coding regions.

Recently, there has been a surge of pre-trained gLMs<sup>20-38,38-43</sup>. gLMs take as input DNA sequences that have undergone tokenization, an encoding scheme applied to either a single nucleotide or *k*-mer of nucleotides. Through self-supervised pre-training, the gLM learns a vector representation for each token in the DNA sequence via masked language modeling (MLM)<sup>1</sup> or causal language modeling (CLM)<sup>44</sup>. In a standard setting of MLM, a portion of the input tokens, typically 15%<sup>1</sup>, is randomly masked, and the task is to predict the masked tokens using the context provided by the rest of the unmasked tokens in the sequence. On the other hand, CLM is an autoregressive pre-training task where the goal is to predict the next token in a sequence given the previous tokens. These language modeling objectives result in learning self-supervised representations of the sequence that capture information about individual tokens and the complex interrelationships between other tokens in the sequence. The burden of learning biologically meaningful features is paid upfront during the pre-training. Afterward, the gLM's representations can be leveraged for a broad spectrum of downstream prediction tasks as inputs to simpler models, bypassing the need to learn essential features for each task from scratch. In contrast, the conventional one-hot representation of DNA sequences treats each element independently, assigning an identical representation for the same nucleotide characters irrespective of their positions in the sequence or what context is nearby. Consequently, the responsibility of extracting important features falls solely on the machine learning model being employed.

Current gLMs are composed of different choices for the tokenization, base architecture, language modeling objective, and pre-training data. *Tokenization* of DNA sequences is employed for either single nucleotide<sup>20-22</sup> or *k*-mer of fixed size<sup>23-25</sup> or a

$k$ -mer of variable sizes via byte-pair tokenization<sup>26,27,45</sup>, which aims to aggregate DNA in a manner that reduces the  $k$ -mer bias in the genome, a problem known as rare token imbalance. The *base architecture* is typically a stack of transformer layers<sup>46</sup>, with a vanilla multi-head self-attention<sup>23–25,27–31</sup> or an exotic attention variant (e.g., flash attention<sup>26,47</sup>, sparse attention<sup>32,33</sup>, or axial attention<sup>34,48</sup>). Alternatively, the base architecture has also been constructed with a stack of residual-connected convolution blocks, either with dilated convolutional layers<sup>20</sup> or implicit convolutions with a Hyena operator<sup>21,22,49</sup>. The *pre-training data* can vary significantly, encompassing the whole genome of a single species<sup>20,24,32</sup> or the whole genomes across multiple species<sup>23,25,26,28,33</sup> or focused only within specific regions of the genomes, such as the untranslated regions (UTRs)<sup>29</sup>, pre-mRNA<sup>30</sup>, promoters<sup>22</sup>, coding regions<sup>35–37</sup>, non-coding RNA<sup>40</sup>, or conserved sites<sup>34</sup>.

Notably, Nucleotide-Transformer<sup>23</sup> is a collection of BERT<sup>1</sup>-style models that consider non-overlapping  $k$ -mer tokenization and is pre-trained via MLM on either a single human genome, a collection of 3,202 human genomes from the 1000 Genomes Project<sup>50</sup> alone or in combination with 850 genomes across diverse species. DNABERT2<sup>26</sup> is also a BERT-style architecture but uses flash attention, considers byte-pair tokenization, and is trained via MLM on the genomes of 850 species. Genomic Pre-trained Network (GPN)<sup>20</sup> is a convolution-based model with a stack of residual-connected dilated convolutions, uses single-nucleotide tokenization, and is trained via MLM on a single Arabidopsis genome. Similarly, HyenaDNA<sup>21</sup> comprises implicit convolution layers, uses single-nucleotide tokenization, and is trained via CLM on the human reference genome. Supplementary Table 1 summarizes the unique combination of components that comprise other gLMs.

The utility of gLMs pre-trained on whole genomes for studying the non-coding genome has been limited. Previous benchmarks have largely considered gLMs that have been fine-tuned (i.e., adjusting the weights of the gLM) on each downstream task<sup>23,24,26,30,40</sup>. In each benchmark, a fine-tuned gLM has demonstrated improved predictions on a host of downstream prediction tasks, often based on the classification of functional elements, such as histone marks or promoter annotations. However, the chosen benchmarks do not reflect the complexity of *cis*-regulatory mechanisms observed in gene regulation, and the baseline models used in the comparisons often do not represent the state-of-the-art. Hence, the capabilities of gLMs in understanding the regulatory genome have yet to be demonstrated in a fair assessment.

Moreover, the reliance on fine-tuning poses challenges, as foundation models are typically large, and fine-tuning on individual tasks demands substantial GPU resources, which may not be readily available to academic labs. Although parameter-efficient fine-tuning methods have emerged, such as LoRA (Low Rank Adaptation)<sup>26,51</sup>, (hard or soft) prompt tuning<sup>21,52</sup>, and (IA)<sup>32,53</sup>, fine-tuning makes it challenging to assess the contribution of the prior knowledge gained via pre-training on each downstream task. Thus, it remains unclear the extent to which existing gLMs pre-trained on whole genomes can genuinely serve as foundation models that can transfer their knowledge to predict and interpret functional genomics data, without necessitating additional fine-tuning of the gLM weights.

Here we perform a focused evaluation to assess the informativeness of learned representations by various gLMs pre-trained on whole genomes (without fine-tuning) for six major functional genomics prediction tasks, which encompass different levels of *cis*-regulation complexity at DNA and RNA levels (see Fig. 1). In particular, we compared the predictive power of representations from pre-trained gLMs – namely Nucleotide-Transformer, DNABERT2, HyenaDNA, and a custom GPN pre-trained on the human reference genome – versus one-hot encoded DNA and representations acquired from a supervised “foundation model” pre-trained on a large corpus of functional genomics data. Our results suggest that current gLMs pre-trained

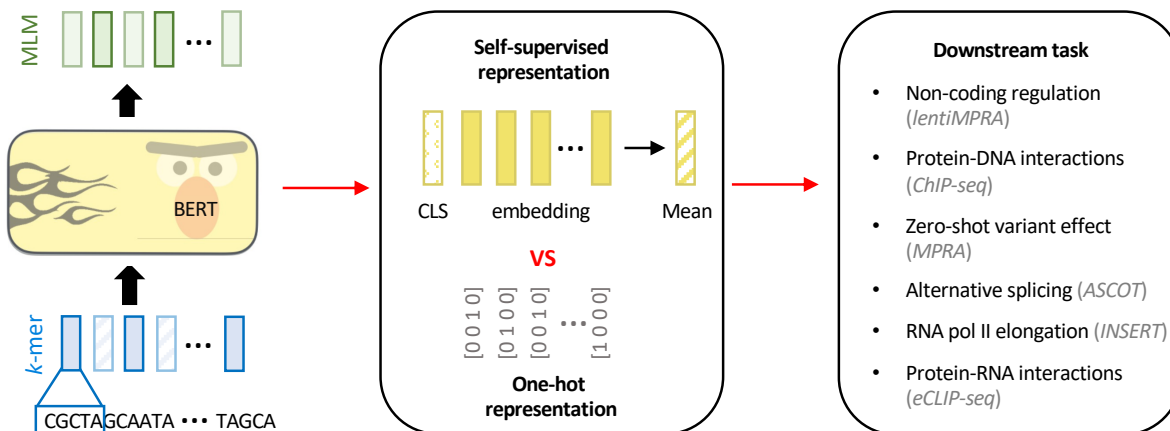


**Figure 1.** Experimental overview. Comparison of gLM embeddings versus one-hot representations for various functional genomics prediction tasks.

on whole genomes do not provide noticeable advantages over conventional approaches to analyzing human functional genomics with deep learning using one-hot sequences. Moreover, supervised foundation models pre-trained on functional genomics data appear to encapsulate more relevant information and transfer better to other functional genomics data, albeit when the source pre-training tasks and the target tasks are closely aligned. Our results suggest that the standard pre-training schemes for current gLMs struggle to understand cell-type specific functional elements and, therefore, fall short of achieving a foundation model status for the non-coding genome of humans.

## Results

### Task 1: Predicting cell-type specific regulatory activity from lentiMPRA data

Understanding the mechanisms that drive CRE activity is a major goal in functional genomics; it is challenging due to complex rules of cell-type-specific TF binding<sup>54,55</sup>. In the first task, we compared the performance of various machine learning models that consider different input representations of DNA sequences at predicting experimentally measured enhancer activity via lentiMPRA (lentiviral Massively Parallel Reporter Assay)<sup>56</sup>. Specifically, this task involves taking a 230 nucleotide (nt) DNA sequence as input, represented either as a gLM embedding or one-hot sequence, and predicting a scalar value that represents the CRE's functional activity measured in a given cellular context via lentiMPRA (see Methods). This task enables a direct comparison in performance across matched downstream models for each sequence encoding scheme. By considering two cell types, namely HepG2 and K562, we can assess whether pre-trained gLM representations capture cell-type-specific CRE activity.

For each gLM, we considered the embeddings from the penultimate layer using a linear model or multi-layer perceptron (MLP) based on the classification token (CLS) or the mean embedding, which is standard practice for harnessing sequence summarization of LLM embeddings. We also employed a baseline convolutional neural network (CNN) that analyzed the full embeddings of the penultimate layer as well as one-hot sequences for comparison (see Methods). We also considered embeddings from the penultimate layer of Sei<sup>57</sup>, a supervised foundation model pre-trained on 21,907 chromatin profiling datasets across over 1,300 cell lines and tissues. To assess the performance against a more sophisticated supervised model, we trained a ResidualBind<sup>58</sup>-like model (ResNet) using one-hot sequences. These choices provide a fair benchmark to assess whether embeddings from foundation models, acquired via unsupervised gLMs or supervised CNNs, are more informative for downstream models than naive one-hot sequences.

We found that CNNs trained on the whole sequence embedding led to improved performance over the linear or MLP models that analyzed CLS or mean embeddings (Fig. 2a). This suggests that summarized gLM representations lack sufficient information to predict cell-type specific regulatory activity, whereas CNNs can build upon the full embeddings to better discriminate cell-type specific features. Moreover, the performance gap between MLPs and linear models suggests that the mapping between the pre-trained representations and the functional readouts of lentiMPRA data is highly non-linear.

We also observed that CNNs trained using sequence embeddings from gLMs generally under-performed standard one-hot sequences, with the exception of our custom-trained GPN (Fig. 2b). Notably, the performance of all gLM-based representations

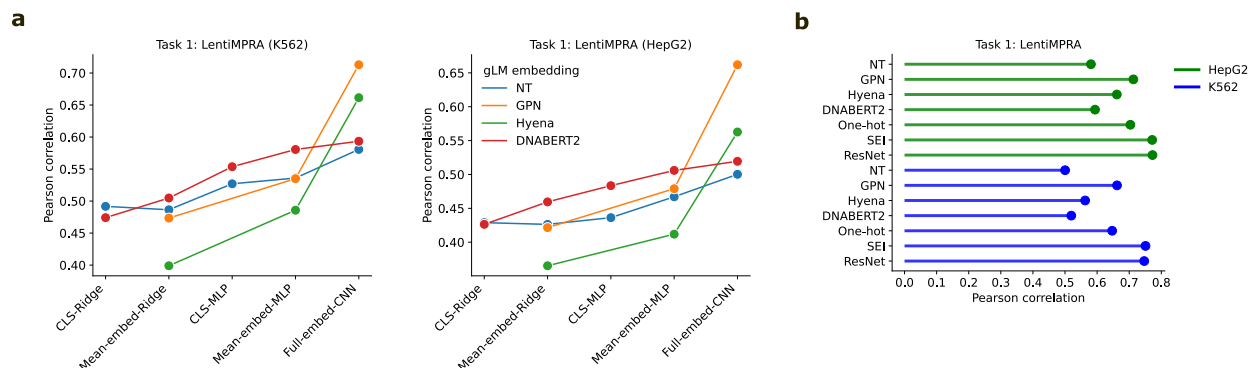


**Figure 2.** Test performance on predicting cell-type-specific regulatory activity from lentiMPRA data. **a**, Comparison of prediction performance across various downstream machine learning models, including ridge regression and MLP using either the gLM's CLS token or mean embedding, and a CNN trained using the full embedding of the penultimate layer of gLMs. **b**, Prediction performance using a baseline CNN trained using different gLM embedding inputs, one-hot sequences, or supervised embeddings from Sei. ResNet represents the performance of a more sophisticated model that is trained using one-hot sequences.

were significantly lower than the supervised representations given by Sei. Due to differences in the data splits for Sei, it is unclear to what extent data leakage might lead to performance inflation. Nevertheless, the ResNet model trained using one-hot sequences on the LentiMPRA dataset also achieved high performance (Fig. 2b). These results suggest that gLM embeddings may not provide beneficial context for CREs that cannot already be learned from one-hot sequences for the lentiMPRA dataset.

To control for the possibility that gLM embeddings from the penultimate layer may not be optimal, we performed the same analysis using embeddings from other layers of Nucleotide-Transformer. While some layers yielded modest improvements, particularly layer 10, the overall trends held and thus did not change the conclusions (Supplementary Fig. 1).

## Task 2: Predicting TF binding sites from ChIP-seq data

Since TF binding is a cell-type-specific phenomenon, but standard language modeling objectives are not cell-type aware, we surmised that the low performance of gLMs on the lentiMPRA prediction task may be due to losing information about key motifs during the pre-training. To test this hypothesis, we evaluated whether the gLM embeddings can predict TF binding sites measured via ChIP-seq (Chromatin Immuno-Precipitation sequencing<sup>59</sup>). Briefly, this task is framed as a binary classification where a model takes a 200 nt DNA sequence, either as a gLM embedding or a one-hot sequence, as input and predicts whether the sequence corresponds to a ChIP-seq peak. We consider ten ChIP-seq datasets spanning different TFs in GM12878 cells; a separate single-task model was trained for each TF (see Methods).

Evidently, CNNs trained using one-hot sequences modestly outperformed the whole embeddings from DNABERT2, HyenaDNA, and Nucleotide-Transformer. On the other hand, the custom GPN occasionally led to improved performance (Fig. 3). Nevertheless, the performance differences across all sequence encoding schemes were modest, suggesting that gLMs do not appear to lose TF-related information in their embeddings. However, it is unclear whether the information provided by gLM embeddings actively encodes for TF motifs or whether the embeddings are simply not losing essential information about the input sequence from which a downstream CNN can learn TF binding information directly from the gLM embeddings, similar to one-hot sequences.

As a control experiment, we trained MLP or linear models using the CLS token of Nucleotide-Transformer. In this way, any information about motifs must be fully encoded in these summarized embeddings. We observed that CNNs trained on the

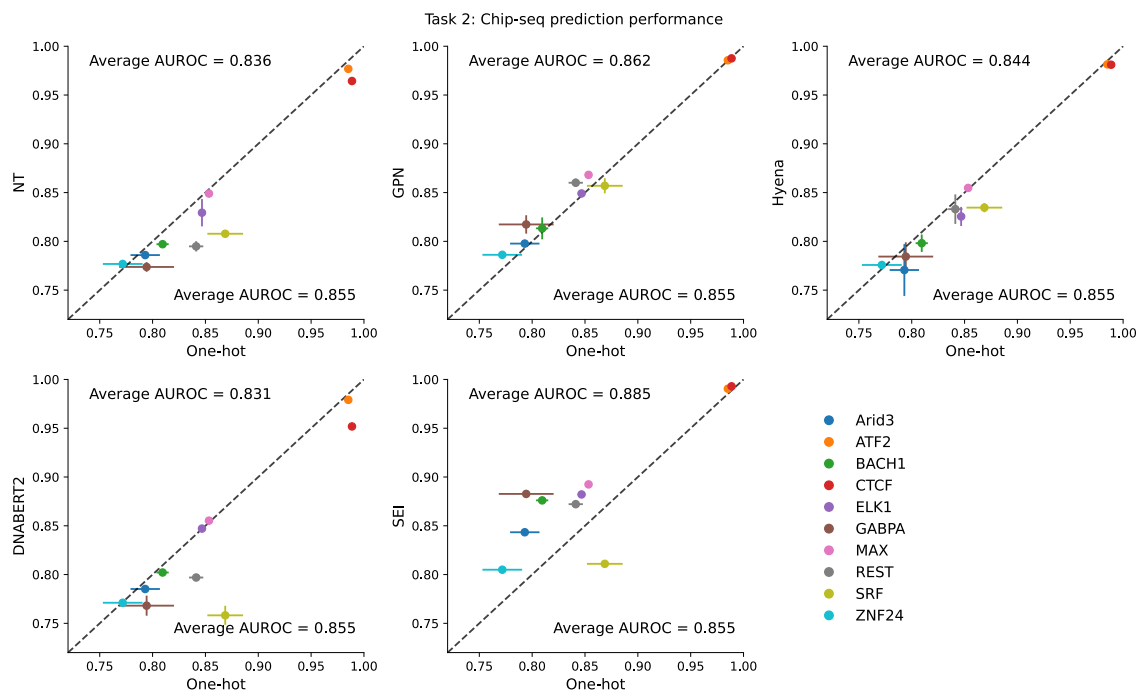


**Figure 3.** Performance comparison on TF binding prediction tasks from ChIP-seq data. Comparisons of CNNs trained using different gLM embeddings versus CNNs trained using one-hot sequences for 10 TF ChIP-seq datasets. Performance is measured by the average area-under the receiver-operating characteristic curve (AUROC) and error bars represent the standard deviation of the mean across 5 different random initializations. Average AUROC represents the average performance across all ChIP-seq datasets.

**Table 1.** Zero-shot variant effect generalization on CAGI5 dataset. The values represent the Pearson correlation between the variant effect predictions with experimental saturation mutagenesis values of a given CRE measured via MPRA. Values are reported for a single CRE experiment for K562 and the average of three CRE experiments for HepG2.

TRAINING TASK	MODEL	VARIANT EFFECT PREDICTION	HEPG2	K562
SELF-SUPERVISED PRE-TRAINING	NT (2B51000G)	COSINE DISTANCE	0.125	0.007
	NT (2B5SPECIES)	COSINE DISTANCE	0.112	0.135
	NT (500MHUMAN)	COSINE DISTANCE	0.020	0.088
	NT (500M1000G)	COSINE DISTANCE	0.041	0.068
	GPN (HUMAN)	LOG2-RATIO	0.002	0.037
LENTIMPRA-EMBEDDING	HYENADNA	COSINE DISTANCE	0.064	0.021
	CNN-GPN	DIFFERENCE FROM WILD TYPE	0.377	0.457
	CNN-NT	DIFFERENCE FROM WILD TYPE	0.137	0.240
LENTIMPRA-ONE-HOT	CNN-SEI	DIFFERENCE FROM WILD TYPE	0.559	0.719
	CNN	DIFFERENCE FROM WILD TYPE	0.313	0.426
	RESIDUALBIND	DIFFERENCE FROM WILD TYPE	0.486	0.551
SUPERVISED ONE-HOT	MPRANN	DIFFERENCE FROM WILD TYPE	0.301	0.369
	SEI	COSINE DISTANCE	0.545	0.641
	ENFORMER (DNASE)	DIFFERENCE FROM WILD TYPE	0.510	0.685

whole embedding yielded substantially higher performance than an MLP trained using the CLS token (Supplementary Fig. 2a). Nevertheless, the MLP still demonstrated aptitude in predicting TF binding overall. To rule out the possibility that biases in the dataset create a trivial prediction task, where low-level sequence statistics can be used to discriminate class labels, we also trained an MLP model on bag-of-dinucleotide frequencies. Indeed, the MLP based on dinucleotide frequencies yielded comparable performance to the CLS token (Supplementary Fig. 2a), except for CTCF, a protein that plays an important role in chromatin structure for all cell types. Together, these results suggest that gLMs do not appear to lose TF-related information in their embeddings, albeit only a slight information boost is gained regarding TF binding compared to low-level dinucleotide statistics. Nevertheless, downstream models that analyze conventional one-hot sequences can easily rectify any information deficiencies, leading to higher performances.

### Task 3: Zero-shot variant effect prediction with MPRA data

A major use case of highly accurate sequence-function models is their ability to predict the functional consequences of non-coding mutations<sup>60</sup>. In previous studies, Nucleotide-Transformer and GPN have demonstrated an ability to predict single-nucleotide variant effects, albeit as part of a binary classification task<sup>20,23</sup>. However, it is not intuitive how gLMs pre-trained on whole genomes could yield good zero-shot predictions of cell-type-specific variant effects in the non-coding region of human genomes since they are trained without any cell-type information. Thus, we assessed the ability of gLMs, specifically Nucleotide-Transformer, GPN, and HyenaDNA, to quantitatively predict single-nucleotide variant effects within CREs using saturation mutagenesis data measured via MPRA (Massively Parallel Reporter Assay)<sup>61</sup>. This task involves calculating the zero-shot variant effect predictions of gLMs either by the cosine similarity of embedding vectors for the input sequence with mutant or wild-type allele (e.g. Nucleotide-Transformer and Hyena) or the log<sub>2</sub>-ratio of predicted variant and wild-type nucleotide via single-nucleotide masking (e.g. GPN). These variant effect scores are compared with experimentally measured variant effects according to the Pearson correlation coefficient (see Methods). This analysis includes MPRA measurements for three CREs in HepG2 cells and one CRE in K562 cells as part of the CAGI5 challenge<sup>61</sup>.

We found that all tested gLMs (without fine-tuning) exhibited poor variant effect predictions in this quantitative zero-shot generalization task (Table 1). These results extended to all Nucleotide-Transformer models<sup>23</sup>, including a 2.5 billion parameter BERT-based gLM trained on 3,202 diverse human genomes and 850 genomes from various species. On the other hand, CNNs trained on lentiMPRA data using gLM embeddings yielded substantially better performance relative to their pre-trained counterparts (Table 1). Moreover, sophisticated models trained using one-hot sequences, such as Enformer<sup>60</sup>, which is a state-of-the-art model trained with supervised learning on a wide variety of functional genomics data using one-hot sequences, and Sei yielded better performance than all CNNs trained using gLM representations. However, the CNN trained using Sei embeddings on the lentiMPRA dataset yielded the best overall performance. Together, these results highlight a major gap in the zero-shot variant effect performance of gLMs with the state-of-the-art.

#### Task 4: Predicting alternative splicing from RNA-seq data

Previous studies demonstrated that Nucleotide-Transformer and GPN has learned properties related to gene definition and splice sites<sup>20,23</sup>. Thus, we surmised that gLMs pretrained on whole genomes may be more beneficial for RNA regulation tasks. To investigate this, we tested the informativeness of gLM embeddings to predict mRNA alternative splicing quantified using RNA-seq (RNA-sequencing) from the ASCOT dataset<sup>62</sup>. Specifically, the prediction task takes as input two sequences – a sequence with 300 nt upstream of the splice acceptor and 100 nt downstream of the acceptor and a sequence with 100 nt upstream of the splice donor and 300 nt downstream of the donor – with the goal of predicting the percentage-spliced-in (PSI) across 56 tissues as a multi-task regression; a task introduced by MTSplice<sup>63</sup>. Similar to the DNA analysis, a baseline CNN was trained to take as input the full embeddings from gLMs or the embeddings of a pre-trained supervised model (see Methods).

Our results mirrored those seen for regulatory DNA, with embedding-based models largely under-performing compared to one-hot-based models (Fig. 4a). In contrast, Sei's embeddings led to substantially lower performance than most gLM embeddings for this task. This is likely due to Sei's pre-training focus on DNA-based functional genomics data, which leads to learning a set of DNA regulatory features that do not transfer well to RNA regulation. To test whether a more relevant set of features acquired through supervised learning could transfer better for RNA regulation, we trained a multi-task ResidualBind-like model to classify RNA-protein binding (RBP) sites from a large trove of eCLIP-seq data (see Methods). The task is to take 1,000 nt sequences as input and predict binding for 120 RBPs in K562 cells as a multi-task classification. Indeed, the embeddings from this RBP-trained supervised model led to substantially better performance than the gLM embeddings, except GPN, which yielded comparable results (Fig. 4a).

#### Task 5: Predicting RNA pol II elongation potential from INSERT-seq data

Next, we performed a similar analysis for a prediction task that takes 173 nt RNA sequences as input and predicts RNA pol II elongation potential measured via INSERT-seq (INtegrated Sequences on Expression of RNA and Translation using high-throughput sequencing)<sup>64</sup>. The INSERT-seq dataset is modest in size, containing only 10,774 sequences. This small data regime may not provide sufficient examples to learn all relevant patterns using one-hot sequences. Training a large deep learning model on this dataset can easily lead to over-fitting. Thus, this task can help evaluate a scenario (i.e., the low data regime) where a baseline CNN that uses gLM embeddings might have an advantage over one-hot sequences.

Similarly, we found that the baseline CNNs trained using gLM embeddings yielded lower performance than one-hot RNA sequences, except for the custom GPN, which performed slightly better (Fig. 4b). Again, the CNN performance based on Sei's supervised embeddings was worse, and the best-performing model was achieved using embeddings from the supervised multi-task model pre-trained to classify RBPs. These results highlight that generic pre-training strategies are not always beneficial; when carefully selecting pre-training tasks, one should consider which relevant features are needed to ensure more positive outcomes on downstream applications.

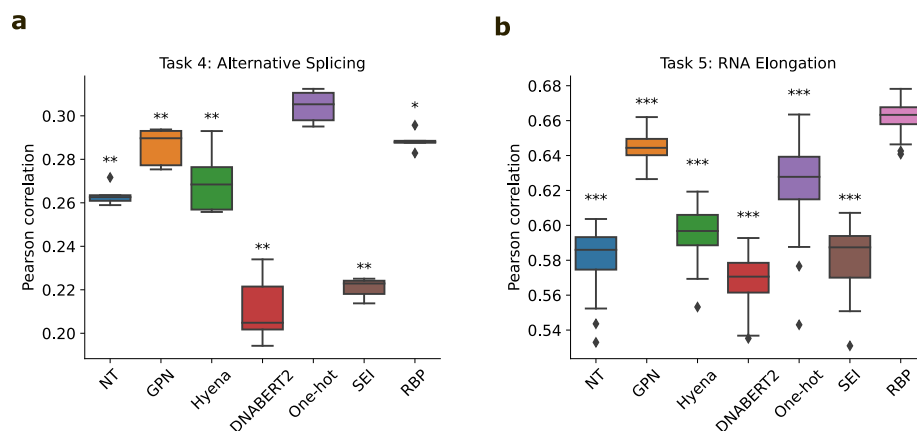


**Figure 4.** Performance on RNA regulation tasks. **a**, Box-plot shows average Pearson correlation across tissues on test data for various models trained with different encoding schemes on an alternative splicing prediction task using MTSplice data. **b**, Box-plot shows Pearson correlation for various models trained with different encoding schemes on a RNA poll II elongation potential prediction task using INSERT-seq data. Box-plots show the first and third quartiles, central line is the median, and the whiskers show the range of data. Box-plots represent 5 different random initializations for **a** and 50 different random initializations for **b**. Statistical significance represents the Mann-Whitney U test with a  $p$  value  $< 0.05$  (\*),  $< 0.01$  (\*\*), and  $< 0.001$  (\*\*\*).

While the custom GPN was the only embedding that demonstrated improved performance over one-hot sequences, we hypothesized that further down-sampling of the training data could lead to situations where gLM embeddings become more beneficial than one-hot sequences. We systematically down-sampled both the alternative splicing and INSERT-seq datasets and retrained the same baseline CNNs using different input encoding schemes. Interestingly, the GPN embeddings consistently outperformed other embeddings (Supplementary Fig. 3). The improved performance by GPN suggests that gLMs may specialize more effectively in specific genomic regions. Specifically in this dataset, capturing 5' splice sites is a critical feature<sup>64</sup>. Thus, understanding what features gLMs learn well can help to identify suitable downstream tasks for which they can thrive.

### Task 6: Predicting RNA-binding protein binding with eCLIP-seq data

RBPs are essential for various RNA processing stages, so next, we examined the ability of gLMs to predict RBP binding sites using eCLIP-seq (enhanced chromatin immunoprecipitation sequencing) datasets<sup>65</sup>. Briefly, the task involves taking 200 nt DNA sequences as input and predicting binary labels of whether the sequence corresponds to an eCLIP-seq peak or not (see Methods). Ten eCLIP-seq datasets spanning different RBPs were used in the evaluation. We trained a baseline CNN model using different sequence encoding schemes similar to previous tasks.

We found that CNNs trained using gLM embeddings performed slightly worse on average compared to the one-hot sequences (Fig. 5a), in agreement with the ChIP-seq results of Task 2. The narrow performance difference between models using gLM embeddings and one-hot sequences also indicates that RBP motif information is not lost in the gLM embeddings. In a similar control, we found that an MLP based on Nucleotide-Transformer's CLS token led to slightly better performance than an MLP based on dinucleotide frequencies (Supplementary Fig. 2b). This supports that gLM embeddings encode beyond low-level sequence statistics in regulatory regions of RNA. Again, we found that Sei embeddings lead to a substantial decline in performance, further highlighting the importance of selecting appropriate pre-training tasks.

### Uncovering cell-type-specific motifs learned by gLMs is challenging

As a follow up, we performed attribution analysis to identify motifs that are captured by gLMs. Attribution maps were generated for a given sequence by systematically masking one input token (i.e., a single nucleotide position for GPN and a

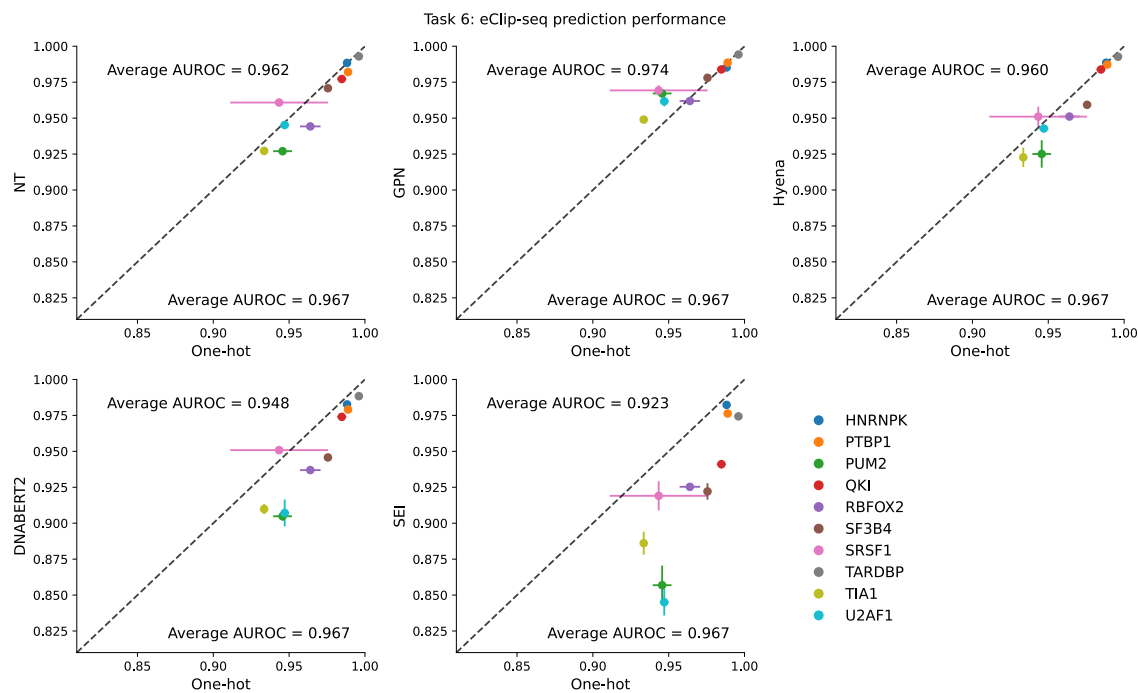


**Figure 5.** Performance comparison on RBP binding prediction tasks from eCLIP-seq data. Comparisons of CNNs trained using different gLM embeddings versus CNNs trained using one-hot sequences for 10 RBP eCLIP-seq datasets. Performance is measured by the average area-under the receiver-operating characteristic curve (AUROC) and error bars represent the standard deviation of the mean across 5 different random initializations. Average AUROC represents the average performance across all eCLIP-seq datasets.

non-overlapping  $k$ -mer for Nucleotide-Transformer) at a time and calculating the entropy over the predicted distribution of the masked token;  $\Delta$ Entropy, which is the difference between the maximum entropy value across the whole sequence and the entropy values at each position, was used to identify positions that yielded informative nucleotides (see Methods). For comparison, we generated gradient-corrected Saliency Maps<sup>66</sup> for a CNN trained using one-hot sequences. The analysis focused on lentiMPRA and CTCF ChIP-seq data to cover tasks from different systems with varying levels of complexity.

As expected, the attribution maps for pre-trained gLMs alone (i.e., not considering the downstream task) were difficult to interpret for both lentiMPRA (Fig. 6a) and ChIP-seq data (Supplementary Fig. 4a). The attribution maps did not reflect any known motifs, nor did they match any of the patterns captured in the CNN's Saliency Maps. This disparity can arise if the

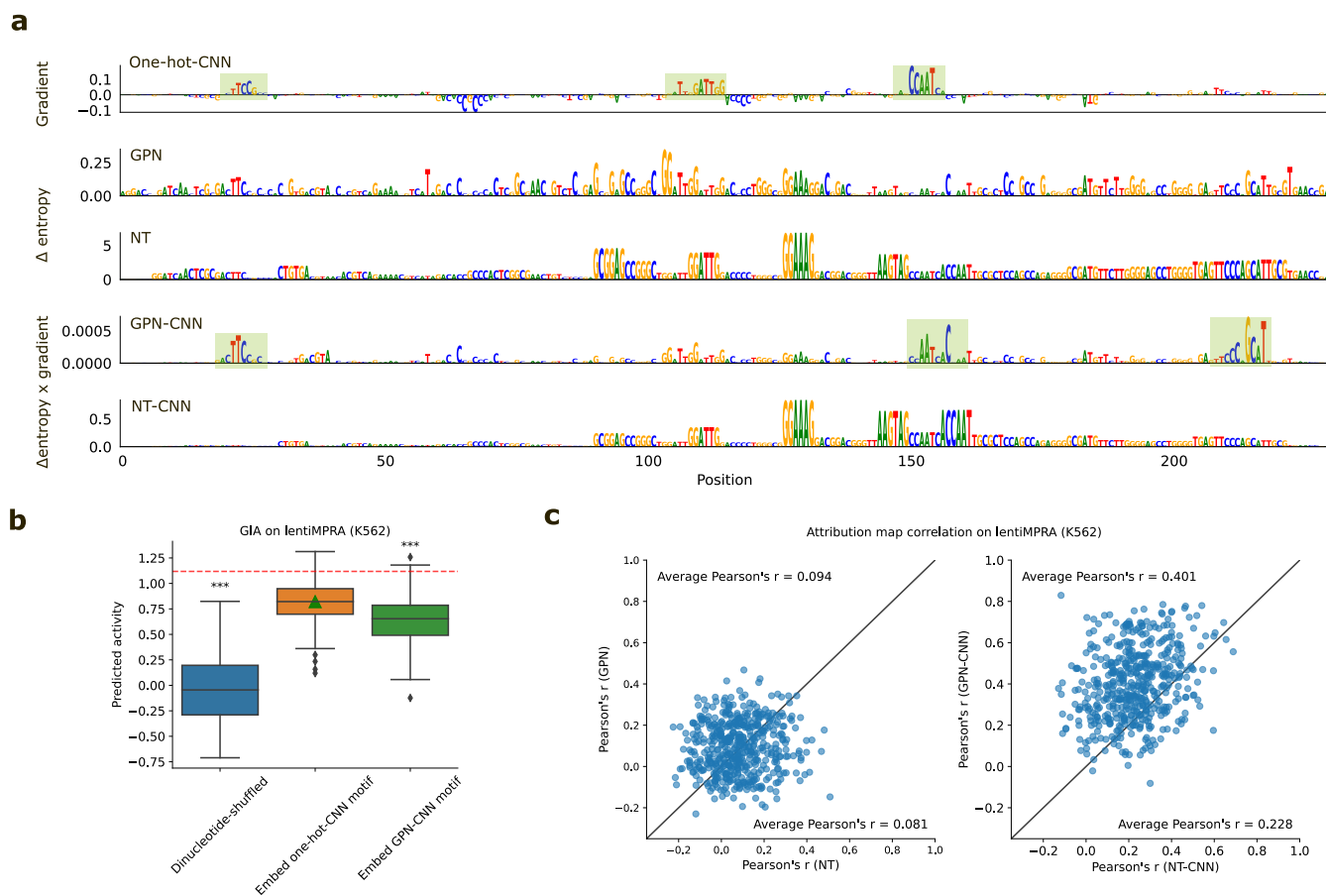


**Figure 6.** Attribution analysis comparison for sequences from the lentiMPRA dataset. **a**, Representative example of attribution maps for a regulatory sequence from the lentiMPRA dataset. Attribution maps include (top to bottom): the gradient-times-input of a one-hot-trained CNN; the delta entropy of predicted nucleotides via single-nucleotide masking from a pre-trained GPN; the delta entropy of predicted nucleotides via single-nucleotide masking from a pre-trained Nucleotide-Transformer; the gradient of a CNN-trained using GPN embeddings multiplied by the delta entropy of predicted nucleotides via single-nucleotide masking from a pre-trained GPN; and the gradient of a CNN-trained using Nucleotide-Transformer embeddings multiplied by the delta entropy of predicted nucleotides via single-nucleotide masking from a pre-trained Nucleotide-Transformer. **b**, Box-plot of the predicted activity for 300 dinucleotide-shuffled sequences from **a**, dinuc-shuffled sequences with the annotated patterns from the Saliency Map of the one-hot-trained CNN, and dinuc-shuffled sequences with the annotated patterns from the CNN trained using GPN embeddings (GPN-CNN). Green triangle represents the global importance analysis value. Red dashed line represents the prediction of the wild type sequence according to the one-hot-trained CNN. Box-plots show the first and third quartiles, central line is the median, and the whiskers show the range of data. **c**, Scatter plot comparison of the attribution map correlations for different pre-trained gLMs (left) and CNNs trained using gLM embeddings (right). Attribution map correlations reflect the Pearson correlation coefficient between the attribution map generated by the gLM-based attribution method with the Saliency Map generated by a one-hot-trained CNN. Each dot represents a different sequence in the lentiMPRA dataset (N=500).



probed locus is used for multiple purposes across different cell types. If cell-type-specific *cis*-regulatory patterns are projected onto a single DNA sequence, the overlapping set of motifs can lead to complex attribution maps that may not resemble distinct cell-type-specific motifs. Alternatively, the complex patterns that seem to span the length of the sequence could also reflect low-level sequence statistics that are memorized. Without ground truth, interpreting attribution maps remains challenging.

Next, we evaluated attribution maps generated by the downstream CNN that used gLM embeddings as input. Specifically, we scaled the gLM's entropy-based attribution map with the maximum gradients at each position based on the downstream CNN (see Methods). Through a qualitative comparison, we noticed that the attribution maps generated by GPN appear to be visually aligned with Saliency Maps generated by the one-hot-trained CNN compared to Nucleotide-Transformer (Fig. 6a), even after accounting for the block-like structure which arises due to the *k*-mer tokenization. This trend was observed for other loci as well (Supplementary Fig. 5).

To validate the importance of the putative binding sites identified via Saliency Maps for the one-hot-trained CNN, we employed global importance analysis (GIA)<sup>58</sup>. Specifically, we embedded the 3 annotated patterns into different dinucleotide-shuffled sequences, which serve as background sequences with low CRE activities, and measured the effect of including the patterns on model predictions. Indeed, GIA shows that the motif patterns identified by Saliency Maps for the one-hot-trained CNN are more-or-less sufficient to explain model predictions (Fig. 6b).

We then quantified the correlation between the attribution maps generated by the one-hot-trained CNN and the gLM-based attribution maps. We found that attribution maps generated by pre-trained gLM are not well-aligned with each other, nor the attribution maps generated by the one-hot-trained CNN (Fig. 6c, Supplementary Fig. 4b). By contrast, attribution maps generated by CNNs trained with gLM embeddings led to improved alignment between their attribution maps and with one-hot-trained CNNs. These results suggest that the gLMs learn non-overlapping features during pre-training, but a downstream model can still use them to build cell-type-specific motifs (that are better aligned with motifs learned by one-hot-trained CNNs).

Together, the attribution maps given by pre-trained gLMs seem to visually capture a more diffuse set of patterns, which speculatively reflect low-level statistics of genomic sequences. Downstream models, like CNNs, appear to use these seemingly uninformative gLM embeddings (especially from GPN) to build cell-type-specific regulatory features that are relevant for downstream prediction tasks.

## Discussion

To assess the transferability of knowledge acquired during pre-training for current genome language models for regulatory genomics, we evaluated four gLMs pre-trained on whole genomes (without fine-tuning) across six functional genomics prediction tasks with appropriate baselines for comparison. We found that the gLM representations provide little to no advantage compared to standard one-hot sequences. On a relative basis, we found that GPN, a convolution-based LLM, yielded slightly more informative representations in the non-coding genome compared to highly parameterized BERT-style LLMs. This suggests that stronger inductive biases toward learning relevant features in the model architecture can improve gLMs, albeit modestly.

Notably, we elected to not fine-tune weights of the gLM on each downstream task, which is how gLMs have been previously benchmarked<sup>23,24,26,30,40</sup>. While gLM performance would likely improve with fine-tuning, the scope of this study was to strictly gauge the knowledge of *cis*-regulatory biology learned during pre-training. The poor performance observed in this study suggests that cell-type-specific *cis*-regulatory mechanisms are predominantly learned during fine-tuning. Our results suggest that the benefit of pre-training gLMs appears to be initializations that are pre-loaded with just a little more information than low-level statistical properties for non-coding genomic sequences.

In previous studies, pre-trained gLMs have found some success by focusing on specific regions of the genome during pre-training or working with simpler organisms with compact genomes<sup>28,34,67</sup>. For instance, a BERT-based LLM trained strictly in the coding genome can provide more context than only considering amino-acids with protein language modeling (e.g., codon usage)<sup>35-37</sup>. However, our evaluation shows that extending the pre-training task across the whole genome struggles to capture meaningful representations in the non-coding genome.

The performance gap may be due to differences in the structure of the coding regions versus the non-coding regions. To elaborate, protein sequences have a clear start and end with low-level grammars (i.e., secondary structures) and high-level grammars (i.e., protein domains) shared throughout most globular proteins, with structures that are conserved across species. On the other hand, the non-coding genome contains a variety of short sequence motifs that vary broadly in binding affinities and are sparsely located in seemingly random DNA, with usage and rules that vary across loci and cell types. Few non-coding elements exhibit deep conservation that is typical in proteins. The differing selection pressures in the non-coding regions lead to loss of synteny, which makes it difficult to study sequence and functional conservation. Thus, treating each nucleotide position equally, whether informative or uninformative, makes this a challenging language modeling task. In the non-coding genome, this is tantamount to expecting the LLM to predict predominantly random nucleotides, which, by definition, can only be achieved via memorization. Hence, this may explain why gLMs have also found greater utility in learning *cis*-regulatory

features in simpler organisms with compact genomes, such as bacteria<sup>41,67</sup>, arabidopsis<sup>20</sup>, or yeast<sup>28</sup>, which have substantially reduced junk DNA<sup>68–70</sup>.

By contrast, supervised deep learning models trained on large troves of functional genomics data in a multitask setting can learn discriminative features related to *cis*-regulatory mechanisms in the non-coding genome<sup>71–75</sup>. However, the representations learned by these models are biased towards the experiments they are trained on, which are predominantly generated within a few cell lines. Hence, their generalization capabilities to other cell types remain limited. A major benefit of gLMs is their lack of reliance on labels generated from wet-lab experiments during training, allowing them to learn a broader set of patterns. However, our results suggest that gLMs have yet to learn a foundational set of *cis*-regulatory features in the non-coding genome of humans that can be harnessed in prediction tasks across cell types.

Evaluating what gLMs have learned through predictive modeling remains an endless endeavor. A more efficient approach can be achieved through model interpretation of the gLMs, which should help to understand the alignment between gLMs and prior biological knowledge. Our preliminary analysis of attribution maps was inconclusive, highlighting the need for a more in-depth understanding of what gLMs are learning from pre-training. Further development of domain-inspired model interpretation tools is needed to bridge this gap.

Looking forward, it remains an open question whether LLMs will bring the same revolution in human genomics as seen in other fields. The current trends in scaling gLMs (via larger models and considering broader sequence contexts<sup>21,32</sup>) might only produce incremental gains, albeit achieved inefficiently according to Chinchilla scaling laws<sup>76</sup>, as the availability of diverse and informative genomics data is a major limiting factor. It remains unclear whether continued scaling of the gLMs pre-trained with standard language modeling objectives (i.e., MLM or CLM) will eventually lead to realizing emergent capabilities, such as learning cell-type-specific *cis*-regulatory biology in the non-coding genome. The amount of genetic variation required to capture the full complexity of the human genome may be simply too great, as a single genome encodes for the spatio-temporal regulation for all cell types. Incorporating additional information, such as functional genomics data, is likely needed during the pre-training for gLMs to become proficient in characterizing cell-type specific functional elements. Even protein language models trained solely on amino-acid sequences can learn elements of conservation and protein structure and yet struggle to generalize well to a wide diversity of functional tasks<sup>77</sup>. In the least, a separate language modeling objective for different regions in the genome to account for the high entropy in the non-coding regions is needed. Due to the high upfront costs to train gLMs with the lack of reciprocal performance gains on downstream tasks, gLMs will likely require a more focused, domain-inspired revelation in pre-training objectives to achieve the esteemed “foundation” status for the non-coding genome.

## References

1. Devlin, J. *et al.* Bert: Pre-training of deep bidirectional transformers for language understanding. *arXiv 1810.04805* (2018).
2. OpenAI. Gpt-4 technical report. *arXiv 2303.08774* (2023).
3. Touvron, H. *et al.* Llama: Open and efficient foundation language models. *arXiv preprint arXiv:2302.13971* (2023).
4. Wei, J. *et al.* Emergent abilities of large language models. *arXiv 2206.07682* (2022).
5. Rives, A. *et al.* Biological structure and function emerge from scaling unsupervised learning to 250 million protein sequences. *Proceedings of the National Academy of Sciences* **118** (2021).
6. Elnaggar, A. *et al.* Prottrans: Toward understanding the language of life through self-supervised learning. *IEEE Transactions on Pattern Analysis and Machine Intelligence* **44** (2021).
7. Madani, A. *et al.* Progen: Language modeling for protein generation. *arXiv preprint arXiv:2004.03497* (2020).
8. Bepler, T. & Berger, B. Learning the protein language: Evolution, structure, and function. *Cell systems* **12**, 654–669 (2021).
9. Lin, Z. *et al.* Language models of protein sequences at the scale of evolution enable accurate structure prediction. *BioRxiv* **2022**, 500902 (2022).
10. Chowdhury, R. *et al.* Single-sequence protein structure prediction using a language model and deep learning. *Nature Biotechnology* **40**, 1617–1623 (2022).
11. Wu, R. *et al.* High-resolution de novo structure prediction from primary sequence. *BioRxiv* 2022–07 (2022).
12. Brandes, N., Goldman, G., Wang, C. H., Ye, C. J. & Ntranos, V. Genome-wide prediction of disease variant effects with a deep protein language model. *Nature Genetics* **55**, 1512–1522 (2023).
13. Meier, J. *et al.* Language models enable zero-shot prediction of the effects of mutations on protein function. *Advances in Neural Information Processing Systems* **34**, 29287–29303 (2021).

14. Madani, A. *et al.* Large language models generate functional protein sequences across diverse families. *Nature Biotechnology* 1–8 (2023).
15. Ferruz, N. & Höcker, B. Controllable protein design with language models. *Nature Machine Intelligence* 4, 521–532 (2022).
16. Hie, B. L. *et al.* Efficient evolution of human antibodies from general protein language models. *Nature Biotechnology* (2023).
17. Hie, B. L., Yang, K. K. & Kim, P. S. Evolutionary velocity with protein language models predicts evolutionary dynamics of diverse proteins. *Cell Systems* 13, 274–285 (2022).
18. Zhang, Z. *et al.* Protein language models learn evolutionary statistics of interacting sequence motifs. *bioRxiv* 2024–01 (2024).
19. Consens, M. E. *et al.* To transformers and beyond: Large language models for the genome. *arXiv 2311.07621* (2023).
20. Benegas, G., Batra, S. S. & Song, Y. S. Dna language models are powerful predictors of genome-wide variant effects. *Proceedings of the National Academy of Sciences* 120, e2311219120 (2023).
21. Nguyen, E. *et al.* Hyenadna: Long-range genomic sequence modeling at single nucleotide resolution. *arXiv preprint arXiv:2306.15794* (2023).
22. Lal, A., Biancalani, T. & Eraslan, G. reglm: Designing realistic regulatory dna with autoregressive language models. In *NeurIPS 2023 Generative AI and Biology (GenBio) Workshop* (2023).
23. Dalla-Torre, H. *et al.* The nucleotide transformer: Building and evaluating robust foundation models for human genomics. *bioRxiv* (2023).
24. Ji, Y. *et al.* Dnabert: pre-trained bidirectional encoder representations from transformers model for dna-language in genome. *Bioinformatics* 37 (2021).
25. Zhang, D. *et al.* Dnagpt: A generalized pretrained tool for multiple dna sequence analysis tasks. *bioRxiv* 2023–07 (2023).
26. Zhou, Z. *et al.* Dnabert-2: Efficient foundation model and benchmark for multi-species genome. *arXiv* (2023).
27. Sanabria, M., Hirsch, J. & Poetsch, A. R. The human genome’s vocabulary as proposed by the dna language model grover. *bioRxiv* 2023–07 (2023).
28. Karollus, A. *et al.* Species-aware dna language models capture regulatory elements and their evolution. *bioRxiv* (2023).
29. Chu, Y. *et al.* A 5’utr language model for decoding untranslated regions of mrna and function predictions. *bioRxiv* 2023–10 (2023).
30. Chen, K. *et al.* Self-supervised learning on millions of pre-mrna sequences improves sequence-based rna splicing prediction. *bioRxiv* (2023).
31. Shen, X. & Li, X. Omnina: A foundation model for nucleotide sequences. *bioRxiv* 2024–01 (2024).
32. Zaheer, M. *et al.* Big bird: Transformers for longer sequences. *Advances in Neural Information Processing Systems* 33, 17283–17297 (2020).
33. Fishman, V. *et al.* Gena-lm: A family of open-source foundational models for long dna sequences. *bioRxiv* 2023–06 (2023).
34. Benegas, G., Albors, C., Aw, A. J., Ye, C. & Song, Y. S. Gpn-msa: an alignment-based dna language model for genome-wide variant effect prediction. *bioRxiv* (2023).
35. Outeiral, C. & Deane, C. M. Codon language embeddings provide strong signals for protein engineering. *bioRxiv* 2022–12 (2022).
36. Hallee, L., Rafailidis, N. & Gleghorn, J. P. cdsbert-extending protein language models with codon awareness. *bioRxiv* (2023).
37. Li, S. *et al.* Codonbert: Large language models for mrna design and optimization. *bioRxiv* (2023).
38. Gündüz, H. A. *et al.* A self-supervised deep learning method for data-efficient training in genomics. *Communications Biology* 6, 928 (2023).
39. Yang, M. *et al.* Integrating convolution and self-attention improves language model of human genome for interpreting non-coding regions at base-resolution. *Nucleic Acids Research* 50, e81–e81 (2022).

40. Chen, J. *et al.* Interpretable rna foundation model from unannotated data for highly accurate rna structure and function predictions. *bioRxiv* (2022).
41. Zvyagin, M. *et al.* Genslms: Genome-scale language models reveal sars-cov-2 evolutionary dynamics. *The International Journal of High Performance Computing Applications* **37**, 683–705 (2023).
42. Levy, B. *et al.* Florabert: cross-species transfer learning with attention-based neural networks for gene expression prediction (2022).
43. Liang, C. *et al.* Rethinking the bert-like pretraining for dna sequences. *arXiv 2310.07644* (2023).
44. Radford, A. *et al.* Language models are unsupervised multitask learners. *OpenAI blog* **1**, 9 (2019).
45. Sennrich, R., Haddow, B. & Birch, A. Neural machine translation of rare words with subword units. *arXiv preprint arXiv:1508.07909* (2015).
46. Vaswani, A. *et al.* Attention is all you need. *Advances in Neural Information Processing Systems* **30** (2017).
47. Dao, T., Fu, D., Ermon, S., Rudra, A. & Ré, C. Flash attention: Fast and memory-efficient exact attention with io-awareness. *Advances in Neural Information Processing Systems* **35**, 16344–16359 (2022).
48. Ho, J., Kalchbrenner, N., Weissenborn, D. & Salimans, T. Axial attention in multidimensional transformers. *arXiv 1912.12180* (2019).
49. Poli, M. *et al.* Hyena hierarchy: Towards larger convolutional language models. *arXiv 2302.10866* (2023).
50. Consortium, . G. P. *et al.* A global reference for human genetic variation. *Nature* **526**, 68 (2015).
51. Hu, E. J. *et al.* Lora: Low-rank adaptation of large language models. *arXiv 2106.09685* (2021).
52. Lester, B., Al-Rfou, R. & Constant, N. The power of scale for parameter-efficient prompt tuning. *arXiv 2104.08691* (2021).
53. Liu, H. *et al.* Few-shot parameter-efficient fine-tuning is better and cheaper than in-context learning. *Advances in Neural Information Processing Systems* **35**, 1950–1965 (2022).
54. Shlyueva, D., Stampfel, G. & Stark, A. Transcriptional enhancers: from properties to genome-wide predictions. *Nature Reviews Genetics* **15**, 272–286 (2014).
55. Zeitlinger, J. Seven myths of how transcription factors read the cis-regulatory code. *Current Opinion in Systems Biology* **23**, 22–31 (2020).
56. Agarwal, V. *et al.* Massively parallel characterization of transcriptional regulatory elements in three diverse human cell types. *bioRxiv* (2023).
57. Chen, K. M., Wong, A. K., Troyanskaya, O. G. & Zhou, J. A sequence-based global map of regulatory activity for deciphering human genetics. *Nature genetics* **54**, 940–949 (2022).
58. Koo, P. K., Majdandzic, A., Ploenzke, M., Anand, P. & Paul, S. B. Global importance analysis: An interpretability method to quantify importance of genomic features in deep neural networks. *PLoS Computational Biology* **17**, e1008925 (2021).
59. Ren, B. *et al.* Genome-wide location and function of dna binding proteins. *Science* **290**, 2306–2309 (2000).
60. Avsec, Ž. *et al.* Effective gene expression prediction from sequence by integrating long-range interactions. *Nature Methods* **18** (2021).
61. Kircher, M. *et al.* Saturation mutagenesis of twenty disease-associated regulatory elements at single base-pair resolution. *Nature Communications* **10** (2019).
62. Ling, J. P. *et al.* Ascot identifies key regulators of neuronal subtype-specific splicing. *Nature Communications* **11** (2020).
63. Cheng, J. *et al.* Mtsplice predicts effects of genetic variants on tissue-specific splicing. *Genome Biology* **22** (2021).
64. Vlaming, H. *et al.* Screening thousands of transcribed coding and non-coding regions reveals sequence determinants of rna polymerase ii elongation potential. *Nature Structural & Molecular Biology* **29** (2022).
65. Van Nostrand, E. L. *et al.* Robust transcriptome-wide discovery of rna-binding protein binding sites with enhanced clip (eclip). *Nature methods* **13**, 508–514 (2016).
66. Majdandzic, A. *et al.* Correcting gradient-based interpretations of deep neural networks for genomics. *Genome Biology* **24** (2023).
67. Nguyen, E. *et al.* Sequence modeling and design from molecular to genome scale with evo. *bioRxiv* (2024).
68. Eddy, S. R. The c-value paradox, junk dna and encode. *Current biology* **22**, R898–R899 (2012).

69. Niu, D.-K. & Jiang, L. Can encode tell us how much junk dna we carry in our genome? *Biochemical and biophysical research communications* **430**, 1340–1343 (2013).
70. Graur, D. *et al.* On the immortality of television sets: “function” in the human genome according to the evolution-free gospel of encode. *Genome Biology and Evolution* **5**, 578–590 (2013).
71. Koo, P. K. & Eddy, S. R. Representation learning of genomic sequence motifs with convolutional neural networks. *PLoS Computational Biology* **15**, e1007560 (2019).
72. Koo, P. K. & Ploenzke, M. Improving representations of genomic sequence motifs in convolutional networks with exponential activations. *Nature Machine Intelligence* **3**, 258–266 (2021).
73. Avsec, Ž. *et al.* Base-resolution models of transcription-factor binding reveal soft motif syntax. *Nature Genetics* **53**, 354–366 (2021).
74. de Almeida, B. P., Reiter, F., Pagani, M. & Stark, A. Deepstarr predicts enhancer activity from dna sequence and enables the de novo design of synthetic enhancers. *Nature Genetics* **54**, 613–624 (2022).
75. Nair, S. *et al.* Transcription factor stoichiometry, motif affinity and syntax regulate single-cell chromatin dynamics during fibroblast reprogramming to pluripotency. *bioRxiv* (2023).
76. Hoffmann, J. *et al.* Training compute-optimal large language models. *arXiv 2203.15556* (2022).
77. Li, F.-Z., Amini, A. P., Yue, Y., Yang, K. K. & Lu, A. X. Feature reuse and scaling: Understanding transfer learning with protein language models. *bioRxiv 2024-02* (2024).
78. Schneider, V. A. *et al.* Evaluation of grch38 and de novo haploid genome assemblies demonstrates the enduring quality of the reference assembly. *Genome Research* **27**, 849–864 (2017).
79. Kingma, D. P. & Ba, J. Adam: A method for stochastic optimization. *arXiv 1412.6980* (2014).
80. Wolf, T. *et al.* Huggingface’s transformers: State-of-the-art natural language processing. *arXiv 1910.03771* (2019).
81. An integrated encyclopedia of DNA elements in the human genome. *Nature* **489**, 57–74 (2012). URL <https://doi.org/10.1038/nature11247>.
82. Yu, F., Koltun, V. & Funkhouser, T. Dilated residual networks. In *Proceedings of the IEEE conference on Computer Vision and Pattern Recognition*, 472–480 (2017).
83. Toneyan, S. *et al.* Evaluating deep learning for predicting epigenomic profiles. *Nature Machine Intelligence* **4** (2022).
84. Tareen, A. & Kinney, J. B. Logomaker: beautiful sequence logos in python. *Bioinformatics* **36**, 2272–2274 (2020).

## Methods

### Pre-trained language models

**Nucleotide-Transformer.** Nucleotide-Transformer consists of multiple BERT-based language models with 2 different model sizes (i.e., 500 million and 2.5 billion parameters) and trained on various sets of genome sequences: human reference genome, 1000 genomes project, and 850 genomes from several species. Details of the tokenizer, model structure, and training procedure can be found in the original paper<sup>23</sup>. We acquired weights for each Nucleotide-Transformer model from the official GitHub repository. In this analysis we mostly used representations from NT2.5B-1000G, except for the zero-shot variant effect generalization analysis, which considered all Nucleotide-Transformer models. Since Nucleotide-Transformer models allow flexible input sizes, no padding was necessary for any evaluation tasks.

**Custom GPN.** The GPN model is a convolutional neural network that was originally trained on Arabidopsis genome sequences via masked language modeling with an input size of 512 nucleotides<sup>20</sup>. It consists of 25 convolutional blocks, where each convolutional block includes a dilated convolutional layer followed by a feed-forward layer, connected by intermediate residual connections and layer normalization. The dilation rate for each convolutional layer cycles with increasing exponentially by factors of 2, from 1 to 32. The embedding dimension was kept fixed at 512 throughout the layers. For our custom GPN (human) model, we created training datasets using the human reference genome (hg38<sup>78</sup>). The genome was split into contigs and filtered for a minimum length of 512 nucleotides, with chromosome 8 held out as test set. During training, 15% of the nucleotide positions were masked and the model is tasked to predict the nucleotide probabilities for each masked location. The model was trained for 2 million steps with a constant learning rate of 0.001 using ADAM<sup>79</sup>.

**HyenaDNA.** The HyenaDNA model is a gLM pretrained on the human reference genome, with context lengths up to 1 million tokens at the single nucleotide-resolution<sup>21</sup>. Architecturally, it adopts a decoder-only, sequence-to-sequence configuration, organized into a succession of blocks each encompassing a Hyena operator<sup>49</sup>, followed by a feed-forward neural network. The model weights and representation extraction code was acquired through the Hugging Face repository<sup>80</sup>. For all experiments in this study, we used the “hyenadna-tiny-1k-seqlen-d256” model due to the sequence length limitation of the functional genomics datasets.

**DNABERT2.** DNABERT2, a second generation version of the original DNABERT model<sup>24</sup>, is constructed on the BERT architecture, comprising 12 Transformer blocks. In this new iteration, the authors improved the model by replacing learned positional embeddings with Attention with Linear Biases (ALiBi) and utilizing Flash Attention to increase computation and memory efficiency<sup>26</sup>. In the context of this study, analyses were done with the representations generated by the last Transformer block. The model was acquired through the Hugging Face repository, using the “DNABERT-2-117M” model.

### Pre-trained supervised models

**Sei.** The Sei model is composed of three sequential modules: (1) a convolutional network with dual linear and nonlinear paths; (2) residual dilated convolution layers; (3) spatial basis function transformation and output layers. Sei was trained to take as input 4 kb length sequences and predict 21,907 TF binding, histone marks and DNA accessibility from peak data of *cis*-regulatory profiles. For this study, we extracted our representations after the spline basis function transformation, before inputting into fully connected layers. The pre-trained Sei model was acquired through zenodo from the original study<sup>57</sup>.

**RBP.** Our custom RBP model was trained using eCLIP-seq<sup>65</sup> data of 120 RBPs in K562 from ENCODE<sup>81</sup>. The dataset was organized into a multi-task binary classification format. The model has a ResidualBind-like structure:

1. 1D convolution (96 filters, size 19, batch-norm, exponential) dropout (0.1)
2. Dilated residual block<sup>82</sup>
  - convolution (96 filters, size 3, batch-norm, ReLU) dropout (0.1)
  - convolution (96 filters, size 3, batch-norm, dilation rate 2) dropout (0.1)
  - convolution (196 filters, size 3, batch-norm, dilation rate 4) dropout (0.1)
  - skip connection to input
  - ReLU activation
  - max-pooling (size 10) dropout(0.1)
3. 1D convolution (192 filters, size 7, batch-norm, ReLU) dropout (0.1) global average-pooling
4. flatten
5. fully-connected (512 units, batch-norm, ReLU) dropout (0.5)
6. output layer (120 units, sigmoid)

### Data

**lentiMPRA.** The lentiMPRA dataset for K562 and HepG2 cell lines was acquired from the Supplementary Tables in Ref.<sup>56</sup>. The HepG2 library consists of 139,984 sequences, each 230 nucleotides long, and the K562 library contains 226,253 sequences. Each sequence is paired with a target scalar value that represents the transcriptional activity. Each cell line was treated independently as a single-task regression. For each dataset, we randomly split the training, validation, and test sets according to the fractions 0.7, 0.1, 0.2, respectively. Unlike the original study, we treated reverse-complement sequences separately; they were not aggregated or augmented during test time. The results represent the performance over a single fold.

**CAGI dataset.** The CAGI5 challenge dataset<sup>61</sup> was used to evaluate the performance of the models on zero-shot single-nucleotide variant effect generalization as following the same procedure as Ref.<sup>83</sup>. We only considered MPRA experiments in HepG2 (LDLT, SORT1, F9) and K562 (PKLR). We extracted 230 nucleotide sequences from the reference genome centered on each regulatory region of interest. Alternative alleles are then substituted correspondingly to construct the CAGI test sequences. Pearson correlation was calculated between the variant effect scores by the model and experimentally measured effect size per experiment. For HepG2 performances, we report the average Pearson’s r across the three experiments.

**ChIP-seq.** Ten transcription factor (TF) chromatin immunoprecipitation sequencing (ChIP-seq) datasets were acquired from the zenodo repository of Ref.<sup>66</sup>. The prediction task is a binary classification of whether 200nt input DNA sequences are associated with a ChIP-seq peak (positive label) versus sequences from DNase I hypersensitive sites from the same cell type (i.e., GM12878) that do not overlap with any ChIP-seq peaks (negative label). The number of negative sequences were randomly down-sampled to exactly match the number of positive sequences to ensure balanced classes. The dataset was split randomly into training, validation, and test set according to the fractions 0.7, 0.1, and 0.2, respectively.

**Alternative splicing data.** Data was acquired from direct correspondence with the authors of Ref.<sup>63</sup>. Briefly, 61,823 cassette exons from ASCOT was split into a training, validation, and test set. The training set consisted of 38,028 exons from chromosome 4, 6, 8, 10-23, and the sex chromosomes. The 11,955 exons from chromosome 1, 7, and 9 were used as the validation set, and the remaining 11,840 exons were used as the test set (chromosomes 2, 3, and 5). Models are evaluated based on their performance on the test set. The prediction task takes as input two sequences – a sequence with 300 nt upstream of the acceptor and 100 nt downstream of the acceptor and a sequence with 100 nt upstream of the donor and 300 nt downstream of the donor – and the goal is to predict PSI across 56 tissues as a multi-task regression.

**INSERT-seq.** INSERT-seq data was obtained from Ref.<sup>64</sup>. INSERT-seq measures the impact of transcribed sequences on the RNA polymerase II elongation potential and expression in mouse embryonic stem cells. 11,417 insert sequences of length 173nt long were used as inputs and the goal is to predict the totalRNA output, which measures the relative abundance in RNA relative to genomic DNA, as a regression task. Training, validation, and test sets were split according to the fractions 0.8, 0.1, and 0.1, resulting in 9,131, 1,149, and 1,137 sequences, respectively.

**eCLIP datasets.** The *in vivo* eCLIP-based datasets were downloaded from the ENCODE. For each RBP experiment, the bed narrowPeaks (two replicates) and the bam file for the corresponding mock inputs experiment were downloaded. For each replicate, we removed peaks with a signal value less than 1 and a  $\log$ - $p$ -value greater than 3. Using bedtools, the remaining peaks that share at least one nucleotide across the two replicates were selected as positive peaks. A correlation filter across the replicates was applied:  $(2(s_i^1 - s_i^2)/(s_i^1 + s_i^2))^2 < 1.0$ , where  $s_i^j$  represent the signal value for the  $i$ th peak in replicate  $j$ . The median peak size was about 50 nt with a positive tail that exceeded 200 nt in some cases. Positive sequences were generated by extracting 200 nucleotide sequences about the center position of the peak coordinates. Sequences with undefined nucleotides were filtered out. Negative peaks were generated by employing Piranha peak caller on the bam file of the mock inputs with a bin size of 20 and a  $p$ -value threshold of 0.01. We then removed negative peaks which overlap with any unfiltered peaks from each replicate. Negative peaks were generated by extracting 200 nt sequences about the center position of the remaining negative peak coordinates. Because the negative peaks usually had more entries compared to the positive peaks, we randomly selected a similar number of negative peaks as positive peaks. All sequences were given a corresponding label 1 for sequences which contain a positive peak and 0 for sequences which contain a negative peak. All sequences were then randomly split into a training set, validation set, and test set according to the fractions 0.7, 0.1, and 0.2, respectively.

## Models for downstream tasks

**Linear models.** Linear models with L2 regularization (i.e., Ridge) serve as the baseline, representing a simple downstream model. The inputs of the model were based on the embeddings of the CLS token or the average embedding across sequences for Nucleotide-Transformer models. For regression and classification tasks, the linear model was a linear regression or logistic regression, respectively. The strength of the L2 regularization was set to  $1e-3$ .

**MLP.** A multi-layer perceptron model was used to train on CLS token embeddings or the average embedding across sequences for Nucleotide-Transformer models. The model is constructed by two fully connected blocks. The first block includes a fully-connected layer with 512 units and ReLU activation, followed by batch-normalization and a dropout rate of 0.5. The second block consists of a fully-connected layer with 256 units and the same activation, batch-normalization, and dropout layers. The model was trained on lentiMPRA dataset with Adam optimizer, learning rate of 0.0001, mean-squared error loss function, learning rate decay with a patience of 5 epochs and a decay factor of 0.2, and early stopping patience of 10 epochs.

**MPRAnn for lentiMPRA.** MPRAnn is a convolutional based model with a total of 4 convolutional and 3 dense layers trained on the lentiMPRA dataset. It takes 230 nt one-hot encoded sequences including the adapters as input to predict the mean  $\log_2(\text{RNA/DNA})$  values from forward and reverse strands. We augmented the batches using the reverse-complement of the 200 nt target sequence, while keeping the two 15 bp adapters fixed. To fit the model, we used a learning rate of 0.001, an early stopping criterion with patience of 10 on 100 epochs, and the Adam optimizer with a mean square error loss function. Model structure and training parameters obtained from Github directory of original publication<sup>56</sup>.

**Baseline CNN for lentiMPRA.** We designed a baseline CNN model with the following structure:

1. batch-norm (optional)

2. 1D convolution (196 filters, size 1) (optional)
3. 1D convolution (196 filters, size 7, batch-norm, exponential)  
dropout (0.2)  
max-pooling (size 5)
4. 1D convolution (256 filters, size 7, batch-norm, ReLU)  
dropout (0.2)  
max-pooling (size 4)
5. flatten
6. fully-connected (512 units, batch-norm, ReLU)  
dropout (0.5)
7. fully-connected (256 units, batch-norm, ReLU)  
dropout (0.5)
8. output layer (1 unit, linear)

CNN models were trained with Adam optimizer, mean-squared error loss function, learning rate of 0.0001 with a learning rate decay patience of 5 epochs with a decay rate of 0.2, and early stopping with patience of 10 epochs for both one-hot sequence and language model embedding-based training on the lentiMPRA dataset. For one-hot sequences, batch-norm and the convolution with kernel 1 were not employed.

**ResidualBind for lentiMPRA.** We designed the ResidualBind model by adding a dilated residual block after the first convolutional layer of the baseline CNN model, according to:

1. 1D convolution (196 filters, size 15, batch-norm, exponential)  
dropout (0.2)
2. Dilated residual block  
convolution (196 filters, size 3, batch-norm, ReLU)  
dropout (0.1)  
convolution (196 filters, size 3, batch-norm, dilation rate 2)  
dropout (0.1)  
convolution (196 filters, size 3, batch-norm, dilation rate 4)  
dropout (0.1)  
convolution (196 filters, size 3, batch-norm, dilation rate 8)  
dropout (0.1)  
convolution (196 filters, size 3, batch-norm, dilation rate 16)  
dropout (0.1)  
convolution (196 filters, size 3, batch-norm, dilation rate 32)  
skip connection to input  
ReLU activation  
max-pooling (size 10)  
dropout(0.2)
3. 1D convolution (256 filters, size 7, batch-norm, ReLU)  
dropout (0.2)  
max-pooling (size 5)
4. flatten
5. fully-connected (512 units, batch-norm, ReLU)  
dropout (0.5)
6. fully-connected (256 units, batch-norm, ReLU)  
dropout (0.5)
7. output layer (1 unit, linear)

ResidualBind was trained with Adam optimizer, mean-squared error loss function, learning rate of 0.001 with a learning rate decay patience of 5 epochs with a decay rate of 0.2, and early stopping with patience of 10 epochs.

**Baseline CNN for ChIP-seq and CLIP-seq.** We designed a baseline CNN model with the following structure:

1. batch-norm (optional)
2. 1D convolution (512 filters, size 1) (optional)
3. 1D convolution (64 filters, size 7, batch-norm, ReLU)  
max-pooling (size 4)  
dropout (0.2)



4. 1D convolution (96 filters, size 5, batch-norm, ReLU)  
max-pooling (size 4)  
dropout (0.2)
4. 1D convolution (128 filters, size 5, batch-norm, ReLU)  
max-pooling (size 2)  
dropout (0.2)
5. flatten
6. fully-connected (256 units, batch-norm, ReLU)  
dropout (0.5)
8. output layer (1 unit, linear)

CNN models were trained with Adam optimizer, binary cross-entropy loss function, learning rate of 0.001 with a learning rate decay patience of 5 epochs with a decay rate of 0.2, and early stopping with patience of 10 epochs for both one-hot sequence and language model embedding-based training on the lentiMPRA dataset. For one-hot sequences, batch-norm and the convolution with kernel 1 were not employed.

**Insert-seq model.** For the RNA pol II elongation potential dataset, we developed a residual convolutional network structure and used it for all embedding and one-hot-based models. The model was trained using mean square error loss function, Adam optimizer, learning rate of 0.0001, learning rate decay patience of 5 epochs with a decay rate of 0.2, and early stopping patience of 10 epochs.

1. convolution(48 filters, size 1) (optional)
2. convolution (96 filters, size 19, batch-norm, exponential)  
dropout (0.1)
3. dilated residual block  
convolution (96 filters, size 3, batch-norm, ReLU)  
dropout (0.1)  
convolution (96 filters, size 3, batch-norm, dilation rate 2)  
dropout (0.1)  
convolution (96 filters, size 3, batch-norm, dilation rate 4)  
skip connection to block input  
ReLU activation  
max-pooling (size 10)  
dropout(0.1)
4. convolution (128 filters, size 7, batch-norm, ReLU)  
global average-pooling  
dropout (0.1)
5. fully-connected layer (128 units, ReLU)  
dropout (0.5)
6. output layer (1 unit, linear)

CNN models were trained with Adam optimizer, mean-squared error loss function, learning rate of 0.0001 with a learning rate decay patience of 5 epochs with a decay rate of 0.2, and early stopping with patience of 10 epochs for both one-hot sequence and language model embedding-based training on the lentiMPRA dataset. For one-hot sequences, the convolution with kernel 1 was not employed.

### Zero-shot variant effect prediction methods

For Nucleotide-Transformer, we derived the zero-shot predictions using cosine similarity as suggested in the original study<sup>23</sup>. For each variant, we passed the sequences with the centered reference allele and the alternative allele through the model to extract embeddings. The cosine similarity between the two complete sequence embeddings was calculated and used as the zero-shot score. A negative correlation is expected between the score and effect size. Since this distance-based zero-shot score only reflects the magnitude, not the direction, of function change, we calculated the Pearson correlation using the absolute value of the effect size.

For GPN, we followed a similar procedure as the original study<sup>20</sup>. First, we input sequences with the center variant loci masked and acquired the predicted allele probabilities for the masked loci. Then, we calculate the zero-shot prediction score as the log-likelihood ratio between the alternate and reference alleles. Again, since the likelihood ratio doesn't reflect the direction of function change associated with the variants, we calculated the correlation score using the absolute value of effect size.

Finally, for the embedding-based and one-hot based models, we used the difference in predictions between the alternative and reference allele sequence as the zero-shot prediction score. For Enformer, we use the cell-type agnostic approach of averaging the effect size across all DNase-seq tracks. To reduce predictions to scalars, we summed across the profile predictions.

### Attribution methods

For CNN models, the attribution analysis was based on grad-times-input with saliency maps. The gradients of the prediction were calculated with respect to the input sequence to yield an  $L \times A$  map, where  $L$  is the length of the sequence and  $A$  is 4 (one for each nucleotide). By subtracting the position-wise average saliency scores from this map and then multiplying by the one-hot encoded sequence, the method isolates the sensitivity of each observed nucleotide at every position, enhancing interpretability by pinpointing nucleotide-specific contributions to predictions.

For gLMs, the analysis involved sequentially masking each token of the input sequence and predicting the probability of the masked token by the model. The entropy of the probability distribution for each position was computed to quantify the information content represented by the gLM. Given that lower entropy signifies a higher information level, the saliency score was derived as the difference between the maximum entropy value and the entropy at each position, ensuring that a higher saliency score reflects greater information retention.

Sequence logos were visualized using Logomaker<sup>84</sup>.

### Global importance analysis

Global importance analysis was carried out according to Ref.<sup>58</sup>. A example sequence was selected from the LentiMPRA (K562) dataset. We sampled 300 dinucleotide shuffled versions of the sequence to be used as background sequences. The shuffling aims to preserve the dinucleotide frequency while destroying any coherent patterns. The LentiMPRA trained One-Hot-CNN models' predictions for the shuffled sequences are considered to be the baseline for predicted CRE activity. The top three positive motif patterns identified separately in the One-hot-CNN and GPN-CNN saliency maps (Fig. 6c) were inserted into the corresponding position of the shuffled sequences, creating two experiment sequences sets. The One-Hot-CNN model was used to make predictions for the motif embedded sequences. The difference in prediction for the three sets of sequences reflect the global importance of these motif patterns to the CNN model.

### Data and Code Availability

Open-source code to reproduce this study can be found at [https://github.com/amberT15/LLM\\_eval](https://github.com/amberT15/LLM_eval). Processed data can be found at: <https://doi.org/10.5281/zenodo.8279716>.

### Acknowledgements

The authors would like to thank Evan Seitz for providing Enformer variant effect predictions and other members of the Koo Lab for helpful comments on the manuscript. Research reported in this publication was supported in part by the National Human Genome Research Institute of the National Institutes of Health under Award Number R01HG012131 and the National Institute Of General Medical Sciences of the National Institutes of Health under Award Number R01GM149921. ZT was also supported by the Elisabeth Sloan Livingston Fellowship. This work was performed with assistance from the US National Institutes of Health Grant S10OD028632-01.

### Author contributions

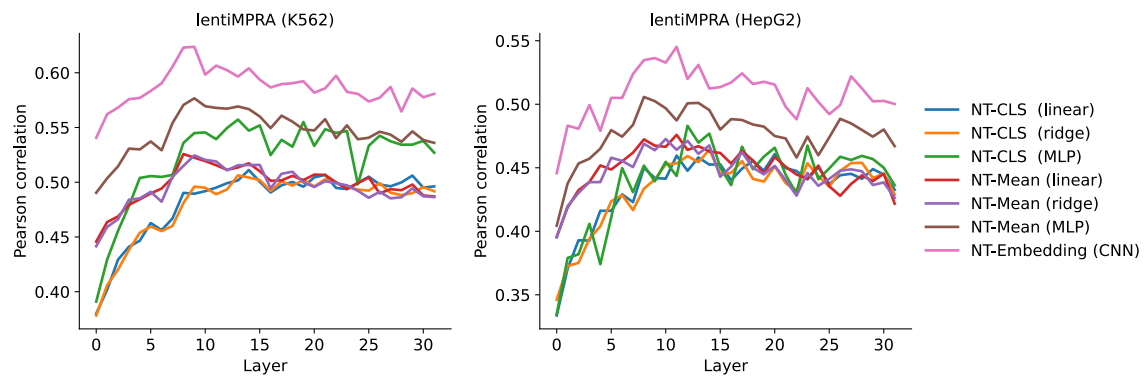
ZT and PKK conceived of the method and designed the experiments. ZT developed code, ran the experiments, and analyzed the results. ZT and PKK interpreted the results and contributed to writing the paper.

### Competing interests

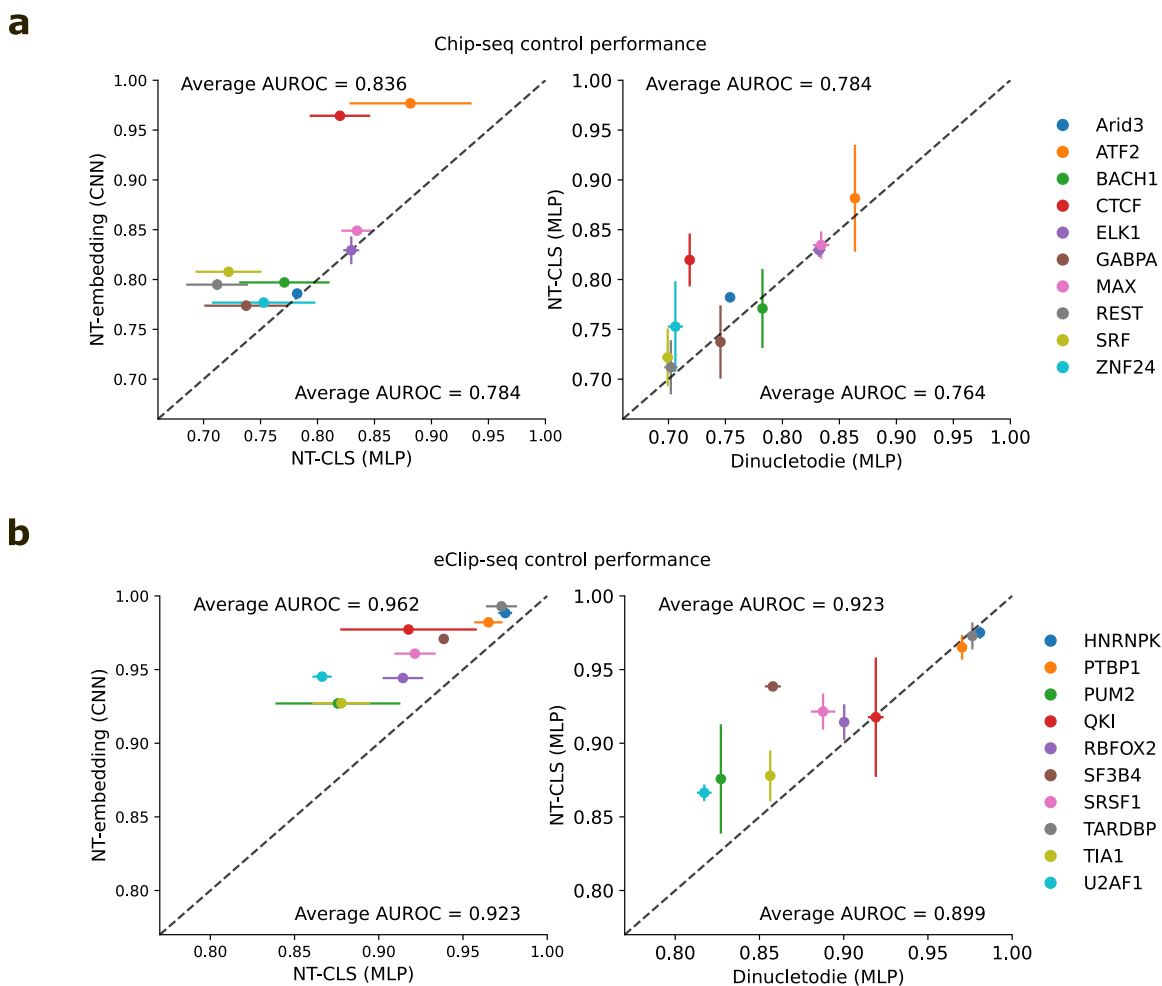
Nothing to declare.

**Supplementary Table 1.** Summary of existing gLM architecture and training choices

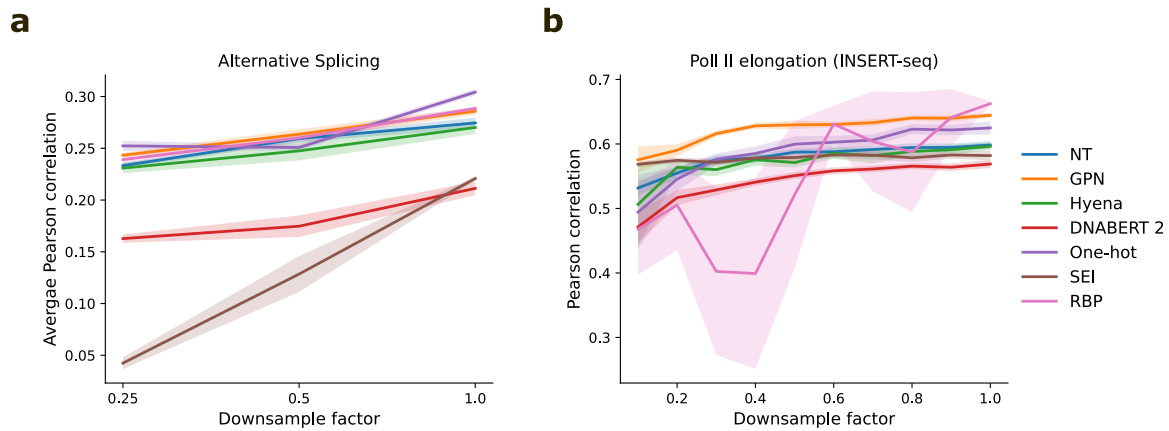
Name	Base Model	Training Data	Pre-training Task	Encoding Scheme	Finetuned for evaluations
GPN [20]	Convolution	Arabidopsis thaliana genome	MLM	Base-res	No
GPN-MSA [34]	Axial attention	Conserved regions in 100 vertebrates MSA (PhastCons)	MLM	Base-res	No
Nucleotide Transformer [23]	BERT	1000 Genomes, Human genome and multi-species genomes	MLM	Non-overlapping k-mer	Yes
DNABERT [24]	BERT	Human genome	MLM	Overlapping k-mer	Yes
DNABERT2 [26]	Flash attention	Human genome and multi-species genomes	MLM	Byte-pair encoding	Yes
BigBird [32]	Sparse attention	Human genome	MLM+CLM	Byte-pair encoding	Yes
hyenaDNA [21]	Hyena	Human genome	CLM	Base-res	Yes
Omnina [31]	LLaMA	Multi-species and text annotations	CLM (multimodal)	Byte-pair encoding	Yes
GENA-LM [33]	BERT	T2T, 1000 Genomes, and multi-species genomes	MLM	Byte-pair encoding	Yes
LOGO [39]	ALBERT	Human genome	MLM	Non-overlapping k-mer	Yes
DNA-GPT [25]	GPT	Genome from 9 species	CLM, GC-content, and sequence order	Non-overlapping k-mer	Yes
GROVER [27]	BERT	Human genome	MLM	Byte-pair encoding	Yes
UTR-LM [29]	BERT	5' UTR sequences (Ensembl)	MLM and supervised (secondary structure and minimum free energy)	Base-res	Yes
SpliceBERT [30]	BERT	pre-mRNA from 72 vertebrates	MLM	Base-res	Yes
regLM [22]	Hyena	Yeast promoter sequences	CLM	Base-res	Yes
RNA-FM [40]	BERT	RNAcentral (promoters)	MLM	Base-res	Yes
Species-aware DNA LM [28]	BERT	UTR of 1500 yeast genomes	MLM	Base-res	No
FloraBERT [42]	BERT	Multi-species plant genome	MLM	Byte-pair encoding	Yes
RandomMask [43]	BERT	Human genome	MLM (expanding size)	Overlapping k-mer	Yes
GenSLMs[41]	BERT	BV-BRC dataset	Contrastive loss	Codon	Yes
Evo [67]	StripedHyena	prokaryotic genomes and plasmids	CLM	Base-res	Both



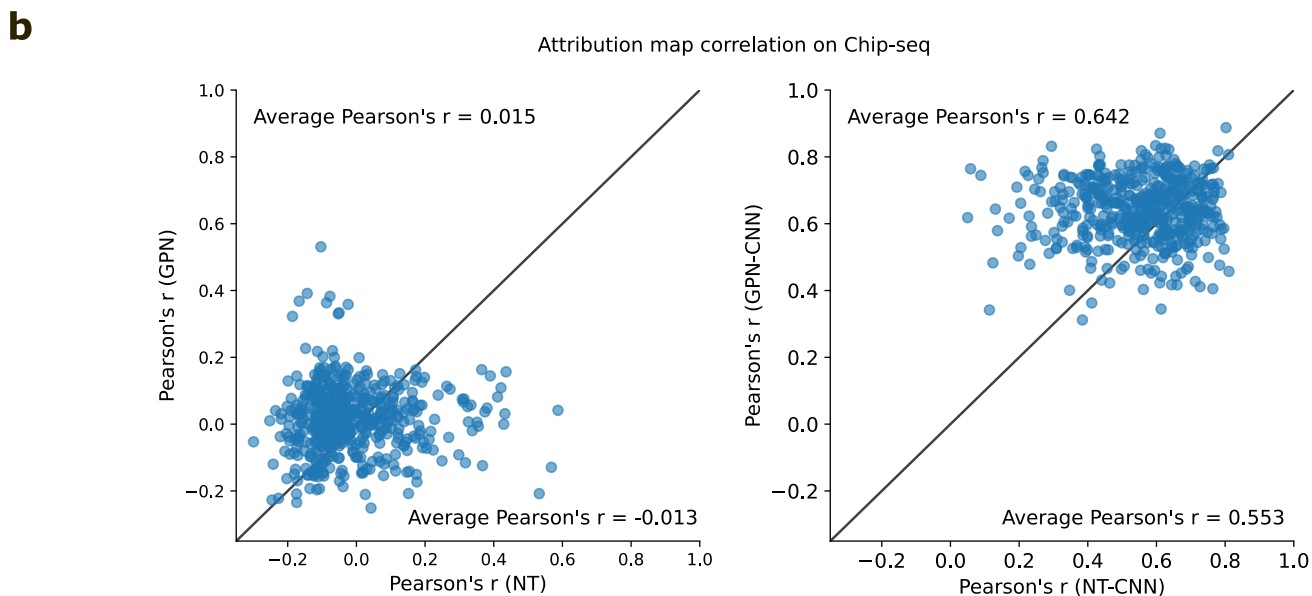
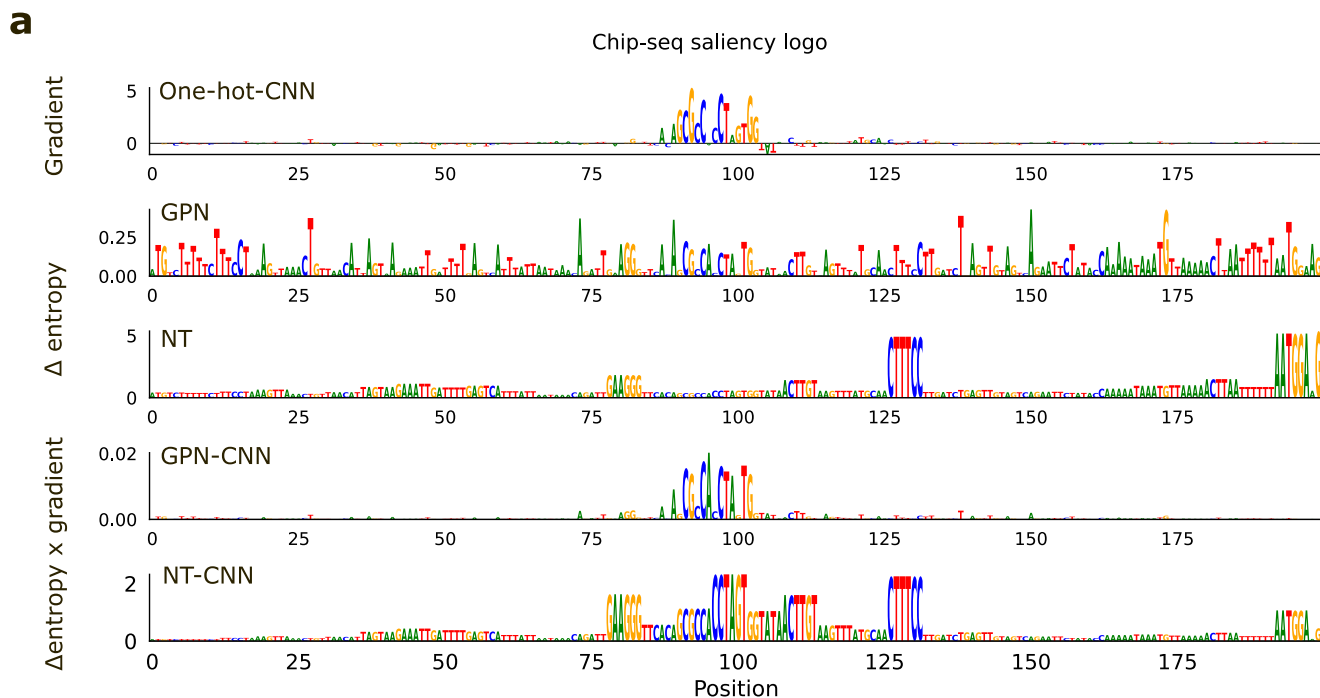
**Supplementary Figure 1.** Layer-wise performance of Nucleotide-Transformer on the lentiMPRA dataset. Test performance of various machine learning models trained using embeddings from different layers of Nucleotide-Transformer. Embeddings include the CLS token, mean embedding (Mean), and the full embedding (Embedding). Machine learning models include linear regression (linear), ridge regression (ridge), multi-layer perceptron (MLP) and a convolutional neural network (CNN).



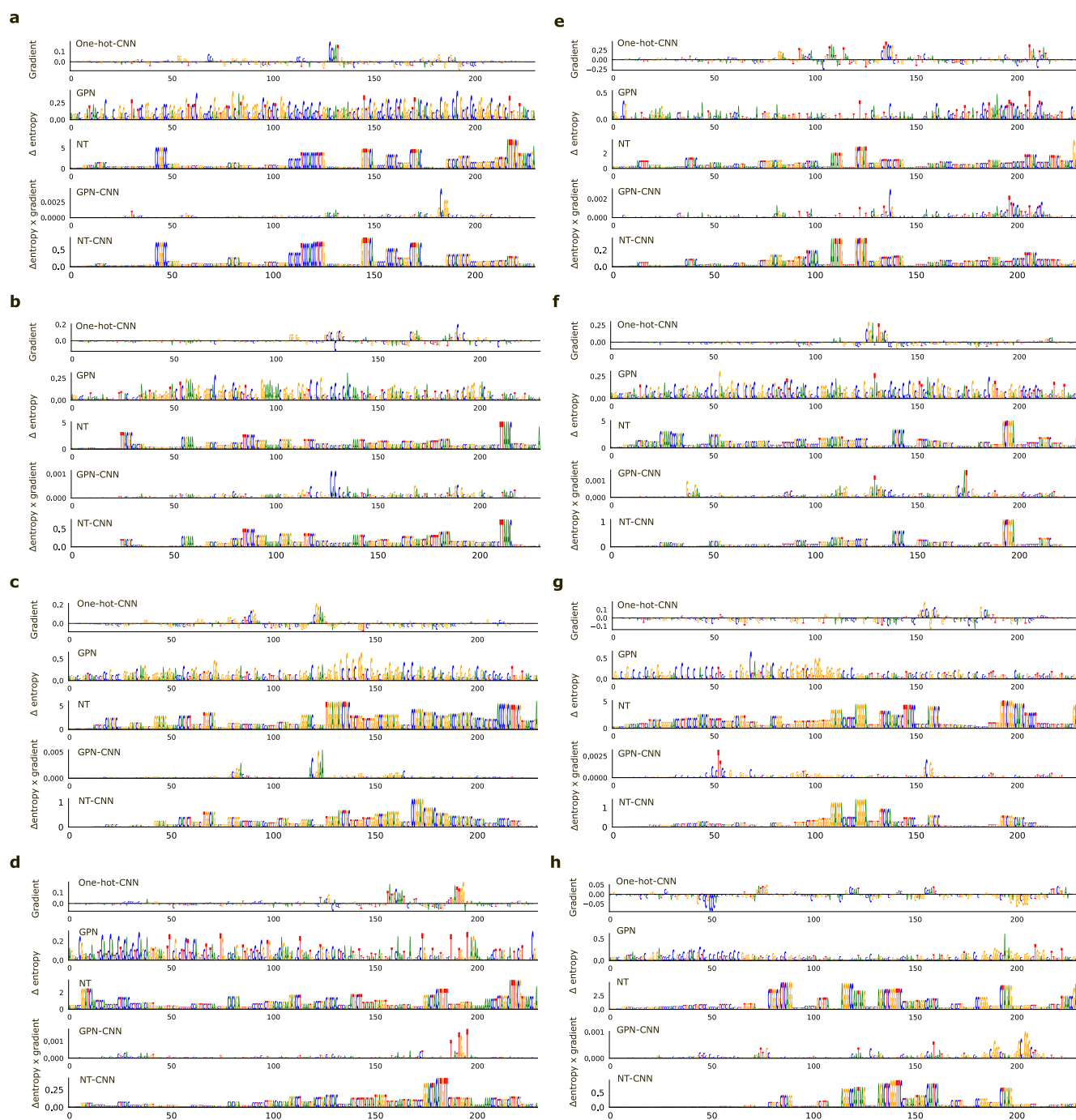
**Supplementary Figure 2.** Control experiments with different embeddings. Performance comparison between a CNN trained using full embeddings of the penultimate layer from Nucleotide-Transformer, an MLP trained using Nucleotide-Transformer's CLS token, and an MLP trained using dinucleotide frequencies of the sequence on (a) ChIP-seq data and (b) eCLIP-seq data. Performance is measured by the average area-under the receiver-operating characteristic curve (AUROC) and error bars represent the standard deviation of the mean across 5 different random initializations. Text values represent the average AUROC across all ChIP-seq or CLIP-seq datasets.



**Supplementary Figure 3.** Down-sampling performance on RNA regulation tasks. Average performance of machine learning models on (a) alternative splicing, task 4, and (b) RNA Pol II elongation potential, task 5, down-sampled by various factors. Shaded region represents standard deviation of the mean across 5 different random initializations.



**Supplementary Figure 4.** Attribution analysis comparison for sequences from CTCF ChIP-seq data. **a**, Representative example of attribution maps for a CTCF binding sequence. Attribution maps include (top to bottom): the gradient-times-input of a one-hot-trained CNN; the delta entropy of predicted nucleotides via single-nucleotide masking from a pre-trained GPN; the delta entropy of predicted nucleotides via single-nucleotide masking from a pre-trained Nucleotide-Transformer; the gradient of a CNN-trained using GPN embeddings multiplied by the delta entropy of predicted nucleotides via single-nucleotide masking from a pre-trained GPN; and the gradient of a CNN-trained using Nucleotide-Transformer embeddings multiplied by the delta entropy of predicted nucleotides via single-nucleotide masking from a pre-trained Nucleotide-Transformer. **b**, Scatter plot comparison of the attribution map correlations for different pre-trained gLMs (left) and CNNs trained using gLM embeddings (right). Attribution map correlations reflect the Pearson correlation coefficient between the attribution map generated by the gLM-based attribution method with the Saliency Map generated by a one-hot-trained CNN. Each dot represents a different sequence in the CTCF ChIP-seq dataset (N=500).



**Supplementary Figure 5.** Representative examples of attribution maps for sequences from the lentiMPRA dataset. In each panel, attribution maps are shown for different sequences in order of (top to bottom): the gradient-times-input of a one-hot-trained CNN; the delta entropy of predicted nucleotides via single-nucleotide masking from a pre-trained GPN; the delta entropy of predicted nucleotides via single-nucleotide masking from a pre-trained Nucleotide-Transformer; the gradient of a CNN-trained using GPN embeddings multiplied by the delta entropy of predicted nucleotides via single-nucleotide masking from a pre-trained GPN; and the gradient of a CNN-trained using Nucleotide-Transformer embeddings multiplied by the delta entropy of predicted nucleotides via single-nucleotide masking from a pre-trained Nucleotide-Transformer.